AGU PUBLICATIONS

Geophysical Research Letters

RESEARCH LETTER
10.1002/2017GL072893

Key Points:
- 3-D simulations predict intense mantle serpentinization and H_2 production at oceanic transform faults
- Rates of serpentinization and H_2 production increase with fault length and are maximum at intermediate slip rates
- Mid-ocean ridges and oceanic transform faults produce similar amounts of H_2 by mantle serpentinization reactions

Correspondence to:
L. H. Rüpke,
lruepke@geomar.de

Citation:
Rüpke, L. H., and J. Hasenclever (2017), Global rates of mantle serpentinization and H_2 production at oceanic transform faults in 3-D geodynamic models, *Geophys. Res. Lett.*, *44*, 6726–6734, doi:10.1002/2017GL072893.

Received 31 JAN 2017
Accepted 28 JUN 2017
Accepted article online 5 JUL 2017
Published online 12 JUL 2017

Global rates of mantle serpentinization and H_2 production at oceanic transform faults in 3-D geodynamic models

Lars H. Rüpke[1] and **Jörg Hasenclever**[1,2]

[1]GEOMAR Helmholtz Centre for Ocean Research Kiel, Kiel, Germany, [2]Faculty of Geosciences, University of Bremen, Bremen, Germany

Abstract Previous studies have estimated that mantle serpentinization reactions generate H_2 at a rate of 10^{10}–10^{12} mol/yr along the global mid-ocean ridge (MOR) system. Here we present results of 3-D geodynamic simulations that predict rates of additional mantle serpentinization and H_2 production at oceanic transform faults (OTF). We find that the extent and rate of mantle serpentinization increases with OTF length and is maximum at intermediate slip rates of 5 to 10 cm/yr. The additional global OTF-related production of H_2 is found to be between 6.1 and 10.7 × 10^{11} mol/yr, which is comparable to the predicted background MOR rate of 4.1–15.0 × 10^{11} mol H_2/yr. This points to oceanic transform faults as potential sites of intense fluid-rock interaction, where chemosynthetic life could be sustained by serpentinization reactions.

1. Introduction

The cycling of seawater through the ocean floor is the dominant mechanism of biogeochemical exchange between the solid Earth and the global ocean. High-temperature black smoker systems found along the global mid-ocean ridge (MOR) system sustain unique ecosystems [*Fisher et al.*, 2007] and are modulators of ocean chemistry on geological time scales [*Kadko et al.*, 1995; *Kump*, 2008]. Hydrothermal exchange also happens at lower temperatures and examples include low-temperature venting at MORs [*Boetius*, 2005], fluid cycling in response to bend faulting at convergent margins [*Ranero et al.*, 2003], and pervasive crustal fluid flow at ridge flanks [*Hutnak et al.*, 2008]. Common to these observations is that crustal fluid flow seems to be associated with major seafloor structures. Oceanic transform faults (OTFs) are one of the most striking, yet poorly understood, features of the global MOR system. Most notable are the OTFs of the slow spreading Mid-Atlantic Ridge (MAR), which shape the ridge structure and reflect continental margin structures along Africa and the Americas.

OTFs are therefore potential sites of substantial biogeochemical exchange. This is particularly interesting with regard to the ocean biome. Deep-sea regions (>2000 m) make up 60% of the Earth's surface, yet the role that deep-sea ecosystems play in global marine biogeochemical cycles is poorly known [*Smith et al.*, 2009]. As a result, fluxes of carbon and biolimiting elements in the deep ocean remain largely unconstrained [*Intergovernmental Panel on Climate Change*, 2013]. Recent observations show that deep marine ecosystems are affected by variations in upper ocean conditions and climate [*Smith et al.*, 2009], which points to a connectedness between deep and upper ocean biogeochemical fluxes. In the light of growing evidence that life is supported by chemosynthesis at hydrothermal vents and within the seafloor below [*Amend et al.*, 2011; *Boetius*, 2005; *Lever et al.*, 2013; *Santelli et al.*, 2008], this opens up the possibility that ocean floor processes may have a notable impact on global marine biogeochemical cycles.

In this context, the serpentine forming interaction between seawater and cold lithospheric mantle rocks is particularly interesting because it is a mechanism of abiotic hydrogen and methane formation [*McCollom and Bach*, 2009; *Seyfried et al.*, 2007], which can support archaeal and bacterial communities at the seafloor [*Kelley et al.*, 2005; *Perner et al.*, 2007; *Shock and Holland*, 2004; *Zhang et al.*, 2016]. Inferring the likely amount of mantle undergoing serpentinization reactions therefore allows estimating the amount of biomass that may be autotrophically produced [*Cannat et al.*, 2010].

Previous estimates of oceanic H_2 production by mantle serpentinization reactions have focused on MORs and are in the range of 10^{10}–10^{12} mol H_2/yr [*Cannat et al.*, 2010; *Emmanuel and Ague*, 2007; *Sleep and Bird*, 2007; *Worman et al.*, 2016]. Such global values are derived by integrating the rate of seafloor production with estimates of the volume of partially serpentinized mantle present within it. *Cannat et al.* [2010] used observations

from individual ridge segments and hydrothermal vent sites to estimate the proportion of serpentine in average slow spreading crust as well as the likely associated H_2 production. Integration of these values with an estimate of the length of slow spreading ridges affected by detachment faulting and mantle exhumation yields a hydrogen production rate of 16.7×10^{10} mol/yr in their preferred scenario. The most recent estimate has been given by *Worman et al.* [2016], who systematically varied the amount of partially serpentinized mantle that may be present within a column of oceanic lithosphere. The resulting model suggests that up to ~10^{12} mol H_2/yr may be produced in oceanic lithosphere when also accounting for off-axis alteration of ocean floor created at intermediate to fast spreading ridges. Such high values would even exceed the most recent estimates for continental H_2 release [*Lollar et al.*, 2014].

Interestingly, a complementary quantitative global assessment of mantle serpentinization and H_2 production at OTFs is still largely missing—despite OTFs having long been hypothesized to be sites of enhanced fluid flow and biogeochemical exchange [*Boschi et al.*, 2013; *Detrick et al.*, 1993; *Francis*, 1981; *Gregg et al.*, 2007; *Roland et al.*, 2010]. Such an analysis requires assessing how the volume of mantle undergoing serpentinization reactions may change toward MOR segment ends and along OTFs. This paper addresses this problem from a mechanistic point of view by investigating a three-dimensional (3-D) numerical chemo-thermo-mechanical model.

A prerequisite for mantle serpentinization to occur is that cold mantle rocks are brought into contact with seawater within the thermal stability limit of serpentine group minerals. At MORs and OTFs this can either occur by the exhumation of ultramafic rocks to the seafloor and/or by crustal-scale brittle faulting that creates fluid pathways for seawater to reach and react with the cold lithospheric mantle. The latter concept had been developed to explain patterns of mantle serpentinization at rifted continental margins [*Bayrakci et al.*, 2016; *Perez-Gussinye and Reston*, 2001; *Rüpke et al.*, 2013]. We here adopt this concept and assume that mantle serpentinization can only occur when the entire oceanic crust is brittle and the mantle rocks beneath are within the thermal stability limit of serpentine. Based on this concept, the new model computes the temperature and deformation field around OTFs and by also resolving the kinetically controlled serpentinization reaction allows making predictions on the likely patterns of mantle serpentinization and H_2 production.

2. Approach

2.1. Viscoplastic Geodynamic Model

We compute the thermal and rheological evolution around a kinematically prescribed OTF that connects two MOR segments with the 3-D finite element thermo-mechanical model M3TET [*Hasenclever*, 2010; *Hasenclever et al.*, 2011]. The visco-plastic flow model incorporates a temperature-dependent viscosity and a plastic yielding criterion. Assuming a Maxwell material in which deformation processes occur in series so that strain rates are cumulative, the effective viscosity, $\eta_{\text{effective}}$, relating stresses to strain rates can be written in terms of the viscous and plastic viscosities:

$$\eta_{\text{effective}} = \left(\frac{1}{\eta_{\text{viscous}}} + \frac{1}{\eta_{\text{plastic}}} \right)^{-1} \tag{1}$$

$$\eta_{\text{viscous}}(T) = \eta_0 \exp\left(\frac{E}{R} \left(\frac{1}{T} - \frac{1}{T_m} \right) \right) \tag{2}$$

$$\eta_{\text{plastic}}(z, \dot{\varepsilon}_{II}) = \frac{\tau_{\max}(z)}{2\dot{\varepsilon}_{II}} \tag{3}$$

$$\tau_{\max}(z) = C_0 + \mu P_{\text{eff}} = C_0 + \mu(\rho_m - \rho_w) g_z z \tag{4}$$

Here T is temperature (°C), z is depth (m), η_0 is the reference viscosity of 10^{19} Pa s at the reference mantle temperature T_m = 1300°C, R = 8.3144598 J/mol/K is the ideal gas constant, and E = 250 kJ/mol is the

activation energy that controls thermally activated creep. $\dot{\varepsilon}_{II}$ (s^{-1}) is the second strain rate invariant, and τ_{max} (Pa) is the plastic yield stress, which depends on cohesion, C_0 = 10 MPa; the friction coefficient, μ = 0.6; and the effective pressure P_{eff}. The latter being here approximated via Terzaghi's effective stress principle as $(\rho_m - \rho_w)g_z z$, where $\rho_m = 3300$ kg/m^3 is mantle density, $\rho_w = 1015$ kg/m^3 is seawater density, and g_z is the vertical gravitational acceleration (m s^{-2}).

This modeling approach is very similar to the one used by *Behn et al.* [2007], who showed that such a model can predict the thermal and rheological evolution of OTFs. Incorporating plastic weakening results in a warmer thermal solution that is more consistent with observed seismicity patterns than the colder solution predicted by earlier Newtonian models [*Behn et al.*, 2007; *Roland et al.*, 2010]. Besides a reference model without hydrothermal cooling (HTC), we have further implemented a parameterization that mimics the cooling effect of fluid circulation through the brittle crust by enhancing the thermal conductivity k:

$$k(z) = k_m + \exp\left(\frac{z}{c}\right)(k_{max} - k_m), \tag{5}$$

where k_m = 3 W/m/K, k_{max} = 24 W/m/K, and c = 500 m is the length scale of decreasing hydrothermal cooling with depth. The used value for k_{max} is equivalent to a Nusselt number of 8, which is a reasonable value over a wide range of spreading rates [*Theissen-Krah et al.*, 2011].

2.2. Serpentinization and H_2 Production Model

Mantle serpentinization processes are simulated by advecting many tracer particles with the solid mantle velocity and computing for each one the changing degree of serpentinization when the particle is within the volume of "serpentinizable" mantle—that is mantle located beneath a crust that deforms by brittle faulting (and not by ductile viscous flow) and is within the thermal stability limit of serpentine formation ($T < 350$°C). Note that a crustal thickness that depends on full spreading rate, u_{full}, is used (2 km if $u_{full} \leq 1$ cm/yr, 3 km if 1 cm/yr $< u_{full} \leqq 2$ cm/yr, 5 km if 2 cm/yr $< u_{full} \leqq 3$ cm/yr, and 6 km if $u_{full} > 3$ cm/yr) consistent with observations [*Bown and White*, 1994]. We have further imposed an upper limit of 15 km sub-Moho serpentinization to stay consistent with the sparse data that is available for OTFs [*Boschi et al.*, 2013] and with observations from different tectonic settings including bend-faults at subduction zones [*Ranero et al.*, 2003; *Van Avendonk et al.*, 2011].

Serpentine group minerals as well as brucite, magnetite, and hydrogen form when cold lithospheric mantle rocks react with seawater at relatively low temperatures [e.g., *Moody*, 1976]. On a grain scale, the reaction rates and products are quite well constrained [*Malvoisin et al.*, 2012; *Martin and Fyfe*, 1970; *Wegner and Ernst*, 1983]. In natural systems, the reaction is more complex, involves multistage reaction pathways, may not necessarily be isochemical [*Malvoisin*, 2015], and is further dependent on fluid composition [*Klein et al.*, 2013]. Resolving mantle serpentinization reactions in lithosphere-scale models therefore requires a certain degree of upscaling. We do this by only considering the hydration of olivine, composed of the solid solution end-members forsterite (90%) and fayalite (10%), along the isochemical reaction pathway given by *Seyfried et al.* [2007]:

$$15Mg_{1.8}Fe_{0.2}SiO_4 + 20.5H_2O \Rightarrow 7.5Mg_3Si_2O_5(OH)_4 + 4.5Mg(OH)_2 + Fe_3O_4 + H_2 \tag{6}$$

We implement this reaction by assuming that its progress is controlled by the temperature-dependent kinetic rate given by

$$f(T) = C_0 A \exp\left(-\frac{b}{T}\right)\left(1 - \exp\left(-c\left(\frac{1}{T} - \frac{1}{T_0}\right)\right)\right), \tag{7}$$

where A = 808.3, b = 3640 K, T_0 = 623.6 K, and c = 8759 K [*Malvoisin et al.*, 2012]. Note that here T is in units of Kelvin. This function peaks at ~300°C and is similar to previous parameterization [*Martin and Fyfe*, 1970; *Wegner and Ernst*, 1983] yet differs from those by being asymmetric and showing a faster drop in reaction rates toward higher temperatures (Figure 1d). $C_0 = 10^{-13}$ s^{-1}scales the normalized reaction rate to a reaction rate with units s^{-1} that is consistent with observations at ultramafic-hosted submarine hydrothermal systems

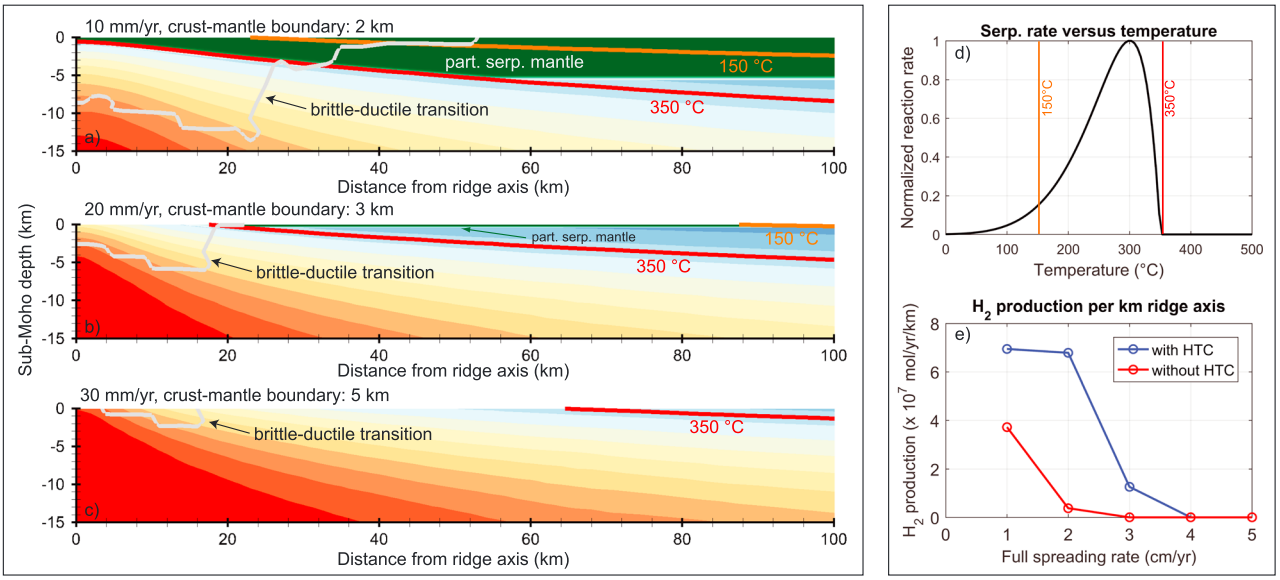

Figure 1. Mantle serpentinization processes at mid-ocean ridges. Mantle serpentinization can occur when the entire crust is brittle and mantle is within the thermal stability field of serpentine formation. (a) At a full spreading rate of 10 mm/yr, mantle serpentinization can occur up to 52 km off-axis and a maximum of 5 km of sub-Moho mantle becomes partially serpentinized. (b) The situation for a full spreading rate of 20 mm/yr. Here the brittle-ductile transition intersects the Moho at about 22 km distance and only ~300 m of sub-Moho mantle become serpentinized. (c) At a full spreading rate of 30 mm/yr, the sub-Moho mantle is too hot where the crust is brittle so that no mantle serpentinization occurs. Figures 1a–1c have been extracted from 3-D simulations and show computed patterns of sub-Moho mantle serpentinization at MOR with different spreading rates. (d) The normalized reaction rate taken from *Malvoisin et al.* [2012] and the temperature window of mantle serpentinization. (e) The modeling results in terms of predicted annual H_2 production rates as a function of MOR spreading rate. Temperature colorbar is the same as in Figure 2.

[*Iyer et al.*, 2012]. The exact value of C_0 is of secondary importance here because on the modeled timescales, the patterns of mantle serpentinization are primarily controlled by temperature and water availability and not by reaction kinetics. We have run additional tests with instantaneous rates and found only small changes in predicted patterns of mantle serpentinization and negligible changes in the predicted H_2 production. The rate of olivine to serpentine conversion can be written as

$$\frac{\partial \rho_{ol}}{\partial t} = -f(T)\rho_{ol} \tag{8}$$

where ρ_{ol} is the remaining amount of olivine in kg/m^3. In all simulations, mantle rocks serpentinize according to equation (8) up to an imposed maximum degree of 50% serpentinization. Equation (6) predicts that 7.48×10^{11} mol H_2 are generated for each cubic kilometer of mantle that serpentinizes to 50% assuming an initial olivine density of 3300 kg/m^3. The imposed upper limit of 50% has been chosen to stay consistent with previously published values of H_2 production per km^3 of mantle rock, which are in the range of $3.5–14 \times 10^{11}$ mol H_2/km^3 [*Worman et al.*, 2016, and references therein].

3. Results

3.1. Mantle Serpentinization at MOR

We first compute a baseline rate of mantle serpentinization and H_2 production at MORs. Figure 1 shows profiles that were extracted from 3-D model runs far away from an OTF. Figure 1a illustrates the modeled mantle serpentinzation patterns at an ultraslow spreading ridge (10 mm/yr full spreading rate). The brittle-ductile transition, which separates plastic (brittle) deformation in the uppermost lithosphere from viscous (ductile) deformation below, intersects the Moho at about 52 km distance to the ridge axis (seafloor age of ~10 Myr) and marks the maximum lateral extent of active mantle serpentinization around the ridge axis. Temperatures are relatively low, so that up to 5 km of sub-Moho mantle is within the thermal stability limit of serpentine production ($T < 350$°C; cf. Figure 1d). The associated integrated rate of H_2 production per kilometer ridge axis between the ridge axis and the maximum lateral extent of mantle serpentinization (52 km,

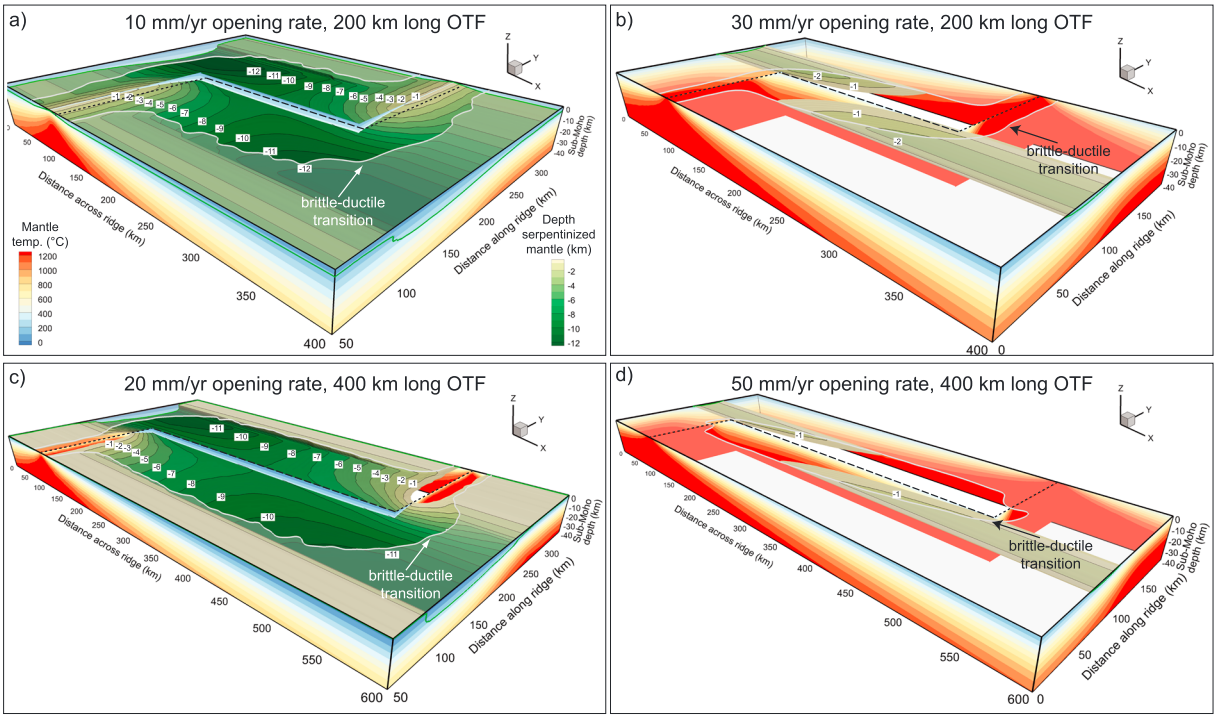

Figure 2. 3-D simulations of mantle serpentinization around oceanic transform faults (OTF). Each panel shows the computed temperature field overlain by the thickness of partially serpentinized sub-Moho mantle. Within the white contour outlines lies the area of crustal-scale brittle deformation. The volume of partially serpentinized mantle increases with fault length and decreases with slip rate. The larger extent of crustal-scale brittle deformation and colder temperatures around OTF lead to a larger volume of mantle becoming serpentinized with respect to the background MOR rate.

~10 Myr) is 3.7×10^7 mol/yr/km. At a higher spreading rate of 20 mm/yr (Figure 1b), the brittle-ductile transition intersects the Moho closer to the ridge axis at ~22 km (seafloor age of ~2 Myr). The 350°C isotherm lies shallower, and only ~300 m of mantle becomes serpentinized implying an integrated annual H_2 production of 0.4×10^7 mol/yr/km. At a full spreading rate of 30 mm/yr (Figure 1c), the brittle-ductile transition intersects the Moho at ~16 km (~1 Myr), but temperatures are too high in the near ridge region for mantle serpentinization reactions, which therefore only occur at MORs spreading at full rates slower than 30 mm/yr in models without HTC (Figure 1e). In simulations including HTC, temperatures are lower and mantle serpentinization can occur at full spreading rates of up to 40 mm/yr (Figure 1e). Global rates of MOR-related H_2 production are calculated by integrating the modeling results with the global distribution of spreading rates [*Bird*, 2003] and are between 4.1×10^{11} and 15.0×10^{11}mol H_2/yr for models with and without HTC, respectively.

3.2. Mantle Serpentinization at OTFs

Figure 2 illustrates how the presence of an OTF can enhance mantle serpentinization. Figure 2a shows the results for an ultraslow slip rate of 10 mm/yr, a fault length of 200 km, and no HTC. The zone of crustal-scale brittle deformation is greatly enhanced around the OTF, and more mantle enters the temperature window of mantle serpentinization (150°C–350°C; Figure 1d) as it cools and moves away from the ridge axis. Up to 12 km of sub-Moho mantle becomes partially serpentinized around the fault zone—more than twice the background MOR value of 5 km. At a faster slip rate of 30 mm/yr, mantle serpentinization only occurs around the OTF (Figure 2b) and not at the adjacent MOR segments. Up to 2 km of sub-Moho mantle becomes serpentinized around the fault zone. Figures 2c and 2d show results for a fault length of 400 km. The longer offset results in a zone of crustal-scale brittle deformation that extends even further off-axis, and the 350°C isotherm is located deeper below the Moho so that more mantle is within the serpentinization window.

We have created two sets of 3-D experiments, each consisting of 55 model calculations, that span the entire range of globally observed slip rates (<180 mm/yr) and fault lengths (10–1100 km): one set without HTC and

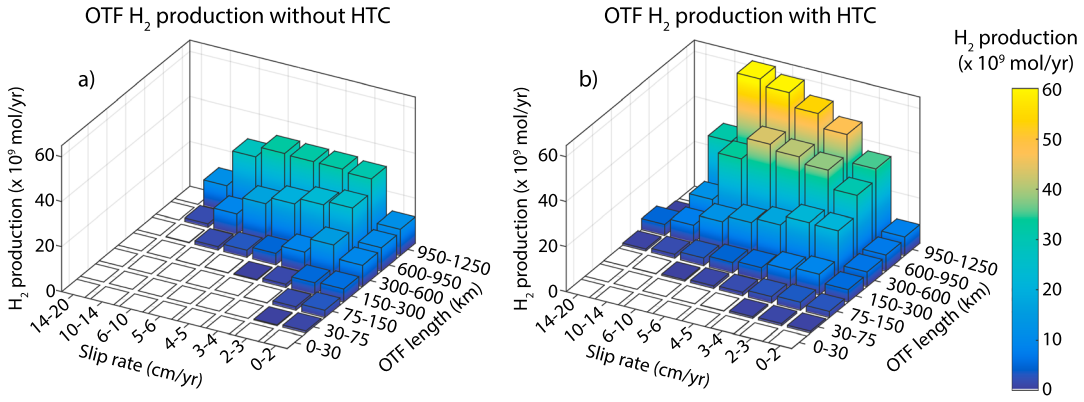

Figure 3. Systematic analysis of H_2 production at OTFs as a function of slip rate and fault length. The shown H_2 production rate is the rate that occurs in addition to the baseline ridge-related production. Each panel is based on 55 3-D simulations.

one with HTC. Figures 3a and 3b show the corresponding rates of OTF-related H_2 production. Note that Figure 3 shows the extra H_2 production that occurs in addition to the baseline MOR value, which is calculated by multiplying the respective rate given in units of mol/yr/km (cf. Figure 1e) with the along-axis MOR length affected by the OTF.

For each slip rate, the OTF-related H_2 production increases with fault length (Figure 3). The reason for this is that crustal-scale brittle deformation (i.e., where water can reach the sub-Moho mantle) extends into progressively older seafloor for increasing fault lengths (Figure 2). As older seafloor has a colder thermal structure, the volume of mantle within the thermal stability limit of serpentine formation increases and thereby the integrated rate of H_2 production. However, a slip rate-dependent minimum fault length exists below which no extra OTF-related H_2 production occurs. This model behavior can be understood by comparing Figure 1 (MORs) and Figures 2 and 3 (OTFs). The 350°C isotherm at an ultraslow (10 mm/yr) MOR intersects the Moho almost directly at the ridge axis and the brittle-ductile transition intersects the Moho at ~52 km distance to the ridge axis (Figure 1a). The distance between these two points marks the "window" of mantle serpentinization. The presence of an OTF with a length significantly shorter than 52 km will not increase this window of mantle serpentinization and will consequently not result in additional H_2 production. At slip rates higher than 30 mm/yr without HTC and higher than 40 mm/yr with HTC (Figure 1e), no MOR-related mantle serpentinization occurs because the brittle-ductile transition intersects the Moho closer to the ridge axis than the 350°C isotherm does (Figure 1). A window of mantle serpentinization only opens up when an OTF of sufficient length moves the location where the brittle-ductile transition intersects the Moho beyond the point where the 350°C isotherm intersects it (Figures 2b and 2d). This distance increases with slip rate and explains why the minimum fault length necessary to produce additional H_2 scales with slip rate.

A higher slip rate further implies a higher flux of mantle through the region of serpentine formation, which increases hydrogen production. But a higher slip rate also results in higher temperatures, which reduces the volume of mantle within the temperature window of serpentine formation. These counteracting mechanisms are the reason that H_2 production at OTFs increases from ultraslow (0–20 mm/yr) to slow (20–50 mm/yr) but decreases again from intermediate (50–80 mm/yr) to fast (>80 mm/yr) slip rates (Figure 3).

3.3. Global Rates of Mantle Serpentinization and H_2 Production

Global rates of additional H_2 production at OTFs are computed by integrating the observed distribution of OTF slip rates and fault lengths (Figure 4a) with our modeling results (Figures 3a and b). The binned annual global H_2 production rates at all OTFs are shown in Figures 4b and 4c for models without and with HTC, respectively. The highest rates of H_2 production occur at ultraslow and slow (without HTC) and at slow to intermediate (with HTC) slip rates and at fault lengths of ~100–800 km. The reason that more H_2 is not produced at OTFs with offsets >800 km is that such long offsets are very rare (Figure 4a). The annual global H_2 production at OTFs is the sum of all bins and is 6.1×10^{11} mol/yr and 10.7×10^{11} mol/yr without and with HTC, respectively.

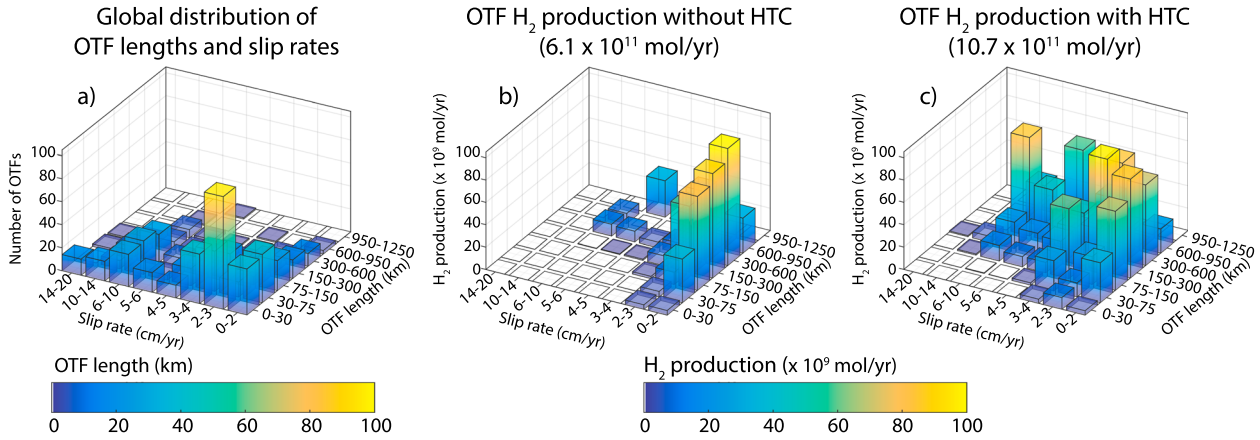

Figure 4. (a) Global distribution of OTFs as a function of slip rate and fault length. (b and c) Global H_2 production rates at OTF without and with parameterized hydrothermal cooling (HTC), respectively. Note that the shown H_2 production rates are the extra production rates that occur in addition to the spreading-related H_2 production at MOR.

4. Discussion

The presented results point to OTFs as sites of intense fluid circulation and mantle alteration. Slow to intermediate slip rates and long fault lengths result in the highest rates of H_2 production. These findings will need to be tested against more data. It is, for example, not clear from geophysical observations how widespread mantle hydration really is at OTFs. The contrasting negative and positive mantle Bouguer anomalies (MBA) of fast- and slow-slipping OTFs are pointing to spreading rate-controlled crustal thickness variations at MOR segment ends and seem to suggest that porosity opening and mantle hydration are limited [*Gregg et al.*, 2007]. Dilatant deformation and mantle serpentinization both result in a density reduction, which needs to be limited for the MBA to remain positive above slow-slipping transforms. This implies that a gravity decrease induced by mantle hydration must be compensated by a gravity increase by crustal thinning. This is consistent with the basic model assumption that mantle hydration is linked to crustal-scale faulting and thereby crustal thinning.

The exceptionally well-studied Vema transform fault on the MAR is an example where mantle serpentinization [*Boschi et al.*, 2013] does seem to be consistent with a positive MBA [*Prince and Forsyth*, 1988]—and it falls into the parameter range for which we predict extensive mantle serpentinization (~300 km offset at ~30 mm/yr slip rate; Figure 3). We also predict that several other prominent OTFs are sites of intense fluid-rock interaction and mantle serpentinization including the Fifteen Twenty (MAR, ~195 km, ~30 mm/yr), Romanche (MAR, 950 km, ~40 mm/yr), and Valdivia (Chile Rise, ~650 km, ~70 mm/yr) transform faults. It will be a matter of future interdisciplinary research to further test the model predictions and to investigate which specific transform faults are sites of intense biogeochemical exchange.

Our predictions on the average baseline global H_2 production rate at MORs are generally consistent with previously predicted values. *Cannat et al.* [2010] estimated that about 20–25% of the seafloor created at ultraslow to slow spreading ridges is made of mantle-ultramafics that partially serpentinize down to a depth of 3–4 km below the seafloor implying an annual hydrogen production of ~1.67×10^{11} mol. Our lower estimate for MOR (without HTC) of 4.1×10^{11} mol H_2/yr is higher. The differences stem from our modeling framework that explores mantle serpentinization in symmetrically spreading ridges (including back-arc spreading centers), while *Cannat et al.* [2010] explicitly tied mantle serpentinization to asymmetric detachment faults at MORs. We also predict a slightly deeper extent of mantle serpentinization of up to ~5 km at ultraslow MORs (Figure 1a) compared to the upper bound of 3–4 km at segment ends estimated by *Cannat et al.* [2010]. Our upper value of 1.5×10^{12} mol H_2/yr at MORs (with HTC) is close to the most recent estimate of ~10^{12} mol H_2/yr by *Worman et al.* [2016]. These two estimate have, however, been derived in different ways. Our upper estimate results from enhanced HTC, which increases the thickness of partially serpentinized mantle in the near-axis region, while *Worman et al.* [2016] investigates the possibility of serpentinization reactions within oceanic lithosphere originally formed at intermediate to fast spreading ridges, which would take place off-axis within older seafloor that has become sufficiently cold.

In total, we predict oceanic H_2 production to be in the range of 10.2–25.7 $\times 10^{11}$ mol/yr, which is the sum of the predicted values for MOR (4.1–15.0 $\times 10^{11}$ mol H_2/yr) and OTF (6.1–10.7 $\times 10^{11}$ mol H_2/yr) with the lower and upper values corresponding to models without and with HTC, respectively. This is consistent with the conclusion reached by *Worman et al.* [2016] that oceanic H_2 production may exceed continental H_2 production, recently estimated to be in the range of 10^{11} mol H_2/yr [*Lollar et al.*, 2014], by up to an order of magnitude. In this context, it should be mentioned that the here presented values are probably an upper bound. One limitation of our modeling approach is that fault zones are not explicitly resolved. Instead water is assumed to be able to reach the mantle wherever the entire crust is brittle. Observations from different tectonic settings including subduction zones and passive continental margins suggest, however, that mantle hydration is often spatially related to specific fault zones [*Bayrakci et al.*, 2016; *Grevemeyer et al.*, 2005; *Ranero et al.*, 2003]. Fluid flow that is restricted to individual fault zones limits the amount available water and thereby the rate of serpentine formation. These considerations necessitate future explorations of numerical models that couple fluid flow, reactions, and deformation.

Our analysis further suggests that similar amounts of H_2 are produced at OTFs and MORs despite their different total lengths (48,000 km versus 67,000 km). The main reason for this is that the models predict that mantle serpentinization at OTFs can occur at higher spreading rates and to a greater depth extent than at MORs (Figures 1 and 3). More than 50% of the global H_2 production at OTFs is nevertheless predicted to occur at full spreading rates $<$30 mm/yr and $<$20 mm/yr for models with and without HTC, respectively. If the combined H_2 production at MORs and OTFs is considered, 50% of it occurs at full spreading rates smaller than about 20 mm/yr. It should be noted here that these findings are based on the assumption that the maximum degree of mantle serpentinization is similar at MORs and OTFs.

Future model-data integration studies are necessary to investigate how deep and widespread mantle hydration at OTFs really is. Despite these uncertainties, our model results do clearly point to OTFs as sites of enhanced fluid flow and biogeochemical exchange. Hydrogen and methane fluxes resulting from mantle serpentinization are known to provide energy to microbial systems [*Kelley et al.*, 2005; *Perner et al.*, 2007; *Shock and Holland*, 2004], so that the here predicted rates can be interpreted as proxies for biomass sustained by fluid-rock interactions. This is particularly interesting in the context of recent observations that suggest that deep ocean ecosystems are affected by variations in the upper ocean conditions and in climate [*Smith et al.*, 2009]. This connectedness may imply that H_2 and CH_4 production by mantle serpentinization reactions at OTFs represents an important missing process in our understanding of global marine biogeochemical cycles.

Acknowledgments
We would like to thank Mark Behn and an anonymous reviewer for their constructive comments that helped to strengthen the manuscript as well as Jeroen Ritsema for the editorial handling. We further thank Karthik Iyer for his insightful suggestions and help. All data for this paper are properly cited and referred to in the reference list. Further details on the numerical modeling and postprocessing procedures as well as additional data files can be obtained from the authors.

References

Amend, J. P., T. M. McCollom, M. Hentscher, and W. Bach (2011), Catabolic and anabolic energy for chemolithoautotrophs in deep-sea hydrothermal systems hosted in different rock types, *Geochim. Cosmochim. Acta*, *75*(19), 5736–5748.
Bayrakci, G., et al. (2016), Fault-controlled hydration of the upper mantle during continental rifting, *Nat. Geosci.*, *9*(5), 384–388.
Behn, M. D., M. S. Boettcher, and G. Hirth (2007), Thermal structure of oceanic transform faults, *Geology*, *35*(4), 307–310.
Bird, P. (2003), An updated digital model of plate boundaries, *Geochem. Geophys. Geosyst.*, *4*(3), 1027, doi:10.1029/2001GC000252.
Boetius, A. (2005), Lost city life, *Science*, *307*(5714), 1420–1422.
Boschi, C., et al. (2013), Serpentinization of mantle peridotites along an uplifted lithospheric section, Mid Atlantic Ridge at 11 degrees N, *Lithos*, *178*, 3–23.
Bown, J. W., and R. S. White (1994), Variation with spreading rate of oceanic crustal thickness and geochemistry, *Earth Planet. Sci. Lett.*, *121*(3–4), 435–449.
Cannat, M., F. J. Fontaine, and J. Escartín (2010), Serpentinization and associated hydrogen and methane fluxes at slow spreading ridges, in *Diversity of Hydrothermal Systems on Slow Spreading Ocean Ridges*, edited by P. A. Rona et al., pp. 241–263, AGU, Washington, D. C.
Detrick, R. S., R. S. White, and G. M. Purdy (1993), Crustal structure of North-Atlantic fracture-zones, *Rev. Geophys.*, *31*, 439–458.
Emmanuel, S., and J. Ague (2007), Implications of present-day abiogenic methane fluxes for the early Archean atmosphere, *Geophys. Res. Lett.*, *34*, L15810, doi:10.1029/2007GL030532.
Fisher, C. R., K. Takai, and N. Le Bris (2007), Hydrothermal vent ecosystems, *Oceanography*, *20*(1), 14–23.
Francis, T. J. G. (1981), Serpentinizing faults and their role in the tectonics of slow spreading ridges, *J. Geophys. Res.*, *86*, 1616–1622.
Gregg, P. M., J. Lin, M. D. Behn, and L. G. Montesi (2007), Spreading rate dependence of gravity anomalies along oceanic transform faults, *Nature*, *448*(7150), 183–187.
Grevemeyer, I., N. Kaul, J. L. Diaz-Naveas, H. W. Villinger, C. R. Ranero, and C. Reichert (2005), Heat flow and bending-related faulting at subduction trenches: Case studies offshore of Nicaragua and Central Chile, *Earth Planet. Sci. Lett.*, *236*(1–2), 238–248.
Hasenclever, J. (2010), *Modeling Mantle Flow and Melting Processes at Mid-Ocean Ridges and Subduction Zones—Development and Application of Numerical Models*, pp. 1–194, Hamburg Univ., Hamburg, Germany.
Hasenclever, J., J. P. Morgan, M. Hort, and L. H. Rüpke (2011), 2D and 3D numerical models on compositionally buoyant diapirs in the mantle wedge, *Earth Planet. Sci. Lett.*, *311*(1–2), 53–68.
Hutnak, M., A. T. Fisher, R. Harris, C. Stein, K. Wang, G. Spinelli, M. Schindler, H. Villinger, and E. Silver (2008), Large heat and fluid fluxes driven through mid-plate outcrops on ocean crust, *Nat. Geosci.*, *1*(9), 611–614.

Intergovernmental Panel on Climate Change (2013), *Climate Change 2013: The Physical Science Basis. Contribution of Working Group I to the Fifth Assessment Report of the Intergovernmental Panel on Climate Change*, pp. 1–1535, Cambridge Univ. Press, Cambridge, U. K., and New York.

Iyer, K., L. H. Rüpke, J. Phipps Morgan, and I. Grevemeyer (2012), Controls of faulting and reaction kinetics on serpentinization and double Benioff zones, *Geochem. Geophys. Geosyst.*, *13*, Q09010, doi:10.1029/2012GC004304.

Kadko, D., J. Baross, and J. Alt (1995), The magnitude and global implications of hydrothermal flux, in *Seafloor Hydrothermal Systems: Physical, Chemical, Biological, and Geological Interactions*, pp. 446–466, AGU, Washington, D. C.

Kelley, D. S., et al. (2005), A serpentinite-hosted ecosystem: The lost city hydrothermal field, *Science*, *307*(5714), 1428–1434.

Klein, F., W. Bach, and T. M. McCollom (2013), Compositional controls on hydrogen generation during serpentinization of ultramafic rocks, *Lithos*, *178*, 55–69.

Kump, L. (2008), The role of seafloor hydrothermal systems in the evolution of seawater composition during the phanerozoic, in *Magma to Microbe: Modeling Hydrothermal Processes at Oceanic Spreading Centers*, edited by R. P. Lowell et al., pp. 275–283, AGU, Washington, D. C.

Lever, M. A., et al. (2013), Evidence for microbial carbon and sulfur cycling in deeply buried ridge flank basalt, *Science*, *339*(6125), 1305–1308.

Lollar, B. S., T. C. Onstott, G. Lacrampe-Couloume, and C. J. Ballentine (2014), The contribution of the Precambrian continental lithosphere to global H-2 production, *Nature*, *516*(7531), 379–382.

Malvoisin, B. (2015), Mass transfer in the oceanic lithosphere: Serpentinization is not isochemical, *Earth Planet. Sci. Lett.*, *430*, 75–85.

Malvoisin, B., F. Brunet, J. Carlut, S. P. Rouméjon, and M. Cannat (2012), Serpentinization of oceanic peridotites: 2. Kinetics and processes of San Carlos olivine hydrothermal alteration, *J. Geophys. Res.*, *117*, B04102, doi:10.1029/2011JB008842.

Martin, B., and W. S. Fyfe (1970), Some experimental and theoretical observations on the kinetics of hydration reactions with particular reference to serpentinization, *Chem. Geol.*, *6*, 185–202.

McCollom, T. M., and W. Bach (2009), Thermodynamic constraints on hydrogen generation during serpentinization of ultramafic rocks, *Geochim. Cosmochim. Acta*, *73*(3), 856–875.

Moody, J. B. (1976), Serpentinization—Review, *Lithos*, *9*(2), 125–138.

Perez-Gussinye, M., and T. J. Reston (2001), Rheological evolution during extension at nonvolcanic rifted margins: Onset of serpentinization and development of detachments leading to continental breakup, *J. Geophys. Res.*, *106*, 3961–3975.

Perner, M., J. Kuever, R. Seifert, T. Pape, A. Koschinsky, K. Schmidt, H. Strauss, and J. F. Imhoff (2007), The influence of ultramafic rocks on microbial communities at the Logatchev hydrothermal field, located 15°N on the Mid-Atlantic Ridge, *FEMS Microbiol. Ecol.*, *61*(1), 97–109.

Prince, R. A., and D. W. Forsyth (1988), Horizontal extent of anomalously thin crust near the Vema fracture-zone from the 3-dimensional analysis of gravity anomalies, *J. Geophys. Res.*, *93*, 8051–8063.

Ranero, C., J. Morgan, K. McIntosh, and C. Reichert (2003), Bending-related faulting and mantle serpentinization at the middle America trench, *Nature*, *425*(6956), 367–373.

Roland, E., M. D. Behn, and G. Hirth (2010), Thermal-mechanical behavior of oceanic transform faults: Implications for the spatial distribution of seismicity, *Geochem. Geophys. Geosyst.*, *11*, Q07001, doi:10.1029/2010GC003034.

Rüpke, L. H., D. W. Schmid, M. Perez-Gussinye, and E. Hartz (2013), Interrelation between rifting, faulting, sedimentation, and mantle serpentinization during continental margin formation-including examples from the Norwegian, *Geochem. Geophys. Geosyst.*, *14*, 4351–4369, doi:10.1002/ggge.20268.

Santelli, C. M., B. N. Orcutt, E. Banning, W. Bach, C. L. Moyer, M. L. Sogin, H. Staudigel, and K. J. Edwards (2008), Abundance and diversity of microbial life in ocean crust, *Nature*, *453*(7195), 653–U657.

Seyfried, W. E., Jr., D. I. Foustoukos, and Q. Fu (2007), Redox evolution and mass transfer during serpentinization: An experimental and theoretical study at 200°C, 500 bar with implications for ultramafic-hosted hydrothermal systems at mid-Ocean ridges, *Geochim. Cosmochim. Acta*, *71*(15), 3872–3886.

Shock, E. L., and M. E. Holland (2004), Geochemical energy sources that support the subsurface biosphere, in *The Subseafloor Biosphere at Mid-Ocean Ridges*, pp. 153–165, AGU.

Sleep, N. H., and D. K. Bird (2007), Niches of the pre-photosynthetic biosphere and geologic preservation of Earth's earliest ecology, *Geobiology*, *5*(2), 101–117.

Smith, K. L., Jr., H. A. Ruhl, B. J. Bett, D. S. M. Billett, R. S. Lampitt, and R. S. Kaufmann (2009), Climate, carbon cycling, and deep-ocean ecosystems, *Proc. Natl. Acad. Sci. U.S.A.*, *106*(46), 19,211–19,218.

Theissen-Krah, S., K. Iyer, L. H. Rüpke, and J. P. Morgan (2011), Coupled mechanical and hydrothermal modeling of crustal accretion at intermediate to fast spreading ridges, *Earth Planet. Sci. Lett.*, *311*(3–4), 275–286.

Van Avendonk, H. J. A., W. S. Holbrook, D. Lizarralde, and P. Denyer (2011), Structure and serpentinization of the subducting Cocos plate offshore Nicaragua and Costa Rica, *Geochem. Geophys. Geosyst.*, *12*, Q06009, doi:10.1029/2011GC003592.

Wegner, W. W., and W. G. Ernst (1983), Experimentally determined hydration and dehydration reaction rates in the system MgO-SiO_2-H_2O, *Am. J. Sci.*, *283-A*, 151–180.

Worman, S. L., L. F. Pratson, J. A. Karson, and E. M. Klein (2016), Global rate and distribution of H_2 gas produced by serpentinization within oceanic lithosphere, *Geophys. Res. Lett.*, *43*, 6435–6443, doi:10.1002/2016GL069066.

Zhang, L., M. Kang, J. Xu, J. Xu, Y. Shuai, X. Zhou, Z. Yang, and K. Ma (2016), Bacterial and archaeal communities in the deep-sea sediments of inactive hydrothermal vents in the Southwest India ridge, *Sci. Rep.*, *6*, 25982.